TABLE OF CONTENTS (TOC)

An Optical Slot-Antenna-Coupled Cavity (SAC) Framework towards Tunable Free-Space Graphene Photonic Surfaces

Sidan Fu,[1] Xiaoxin Wang,[1] Haozhe Wang,[2] Xiaoxue Gao,[1] Kurt Broderick,[2] Jing Kong,[2]* and Jifeng Liu [1]*

1 Thayer school of Engineering, Dartmouth College, 14 Engineering Drive, Hanover, New Hampshire 03755, USA.

2 Department of Electrical Engineering and Computer Science, Massachusetts Institute of Technology, 77 Massachusetts Avenue, Cambridge, Massachusetts 02139, USA.

Page Numbers. The font is ArialMT 16 (automatically inserted by the publisher)

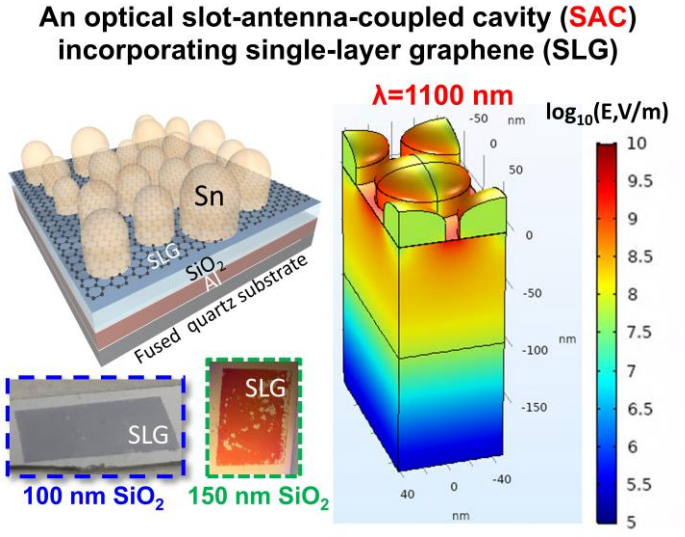

We introduce an optical slot-antenna-coupled cavity (SAC) framework, simultaneously enhancing the absorption of atomically thin single-layer graphene by up to 20x and potentially enabling its electrical gating as a step towards tunable 2D photonic surfaces. This framework synergistically integrates near-field enhancement induced by ultrahigh refractive index semimetal slot-antenna with broadband cavity resonances in visible and infrared regimes, far exceeding the performance of conventional optical antennas or Fabry-Perot cavities alone.

Nano Res (automatically inserted by the publisher)
DOI (automatically inserted by the publisher)
Research Article

An Optical Slot-Antenna-Coupled Cavity (SAC) Framework towards Tunable Free-Space Graphene Photonic Surfaces

Sidan Fu,[1] Xiaoxin Wang,[1] Haozhe Wang,[2] Xiaoxue Gao,[1] Kurt Broderick,[2] Jing Kong,[2] ✉ and Jifeng Liu[1] ✉

[1] Thayer school of Engineering, Dartmouth College, 14 Engineering Drive, Hanover, New Hampshire 03755, USA.

[2] Department of Electrical Engineering and Computer Science, Massachusetts Institute of Technology, 77 Massachusetts Avenue, Cambridge, Massachusetts 02139, USA.

Received: day month year / Revised: day month year / Accepted: day month year (automatically inserted by the publisher)

ABSTRACT

The optical conductivity of single layer graphene (SLG) can be significantly and reversibly modified when the Fermi level is tuned by electrical gating. However, so far this interesting property has rarely been applied to free-space 2D photonic devices because the surface-incident absolute absorption of SLG is limited to 1-2%. No significant change in either reflectance or transmittance would be observed even if SLG is made transparent upon gating. To achieve significantly enhanced surface-incident optical absorption in SLG in a device structure that also allows gating, here we embed SLG in an optical slot-antenna-coupled cavity (SAC) framework, simultaneously enhancing SLG absorption by up to 20x and potentially enabling electrical gating of SLG as a step towards tunable 2D photonic surfaces. This framework synergistically integrates near-field enhancement induced by ultrahigh refractive index semimetal slot-antenna with broadband resonances in visible and infrared regimes, ~3x more effective than a vertical cavity structure alone. An example of this framework consists of self-assembled, close-packed Sn nanodots separated by ~10 nm nanogaps on a SLG/SiO_2/Al stack, which dramatically increases SLG optical absorption to 10-25% at λ=600-1900 nm. The enhanced SLG absorption spectrum can also be controlled by the insulator thickness. For example, SLG embedded in this framework with a 150 nm-thick SiO_2 insulating layer displays a distinctive red color in contrast to its surrounding regions without SLG on the same sample under white light illumination. This opens a potential path towards gate-tunable spectral reflectors. Overall, this work initiates a new approach towards tunable 2D photonic surfaces.

KEYWORDS

Optical slot-antenna-coupled cavity (SAC), Ultrahigh refractive index, Graphene, Photon management, Tunable 2D photonic surfaces

Address correspondence to Jifeng Liu, Jifeng.Liu@Dartmouth.edu; Jing Kong, jingkong@mit.edu.

1. Introduction

Single layer graphene (SLG) attracts a lot of attention from the photonics community for applications in advanced photo-detection [1], image sensing [2], and energy harvesting devices [3]. Specially, the π electrons in the two dimensional (2D) hexagonal lattice demonstrate a unique conical band structure [4, 5]. The zero bandgap of SLG and consequently the very broad inter-band absorption spectrum makes SLG attractive for broadband infrared (IR) photonic devices. More interestingly, this optical absorption spectrum can be significantly and reversibly modified by tuning the Fermi level of SLG through electrical gating [6]. Since the first demonstration of gate-variable optical transitions in SLG [6], applications in waveguide-coupled optical modulators have been investigated extensively, achieving broadband and ultrafast photonic modulation [7-9] for optical communications.

In contrast to waveguide-coupled modulators where light travels parallel to the SLG plane, gate-tunable surface-incident 2D photonic surfaces based on SLG have rarely been reported even though they have great potential applications in tunable optical reflectors/filters/attenuators, as well as high-speed low-power optical switches to substitute their micro-electromechanical (MEMS) counterparts. This is because the surface-incident optical absorption of free-standing SLG is limited to ~2.3% due to its atomic thickness, and it becomes even smaller when SLG is placed onto a substrate due to optical impedance mismatch (i.e. ~1.4% for a SLG placed on fused quartz substrate) [10, 11] Consequently, the free-space transmittance or reflectance can be increased by ~2% at most even when SLG is made transparent upon electrical gating, too small for any practical applications. Therefore, for a tunable free-space 2D photonic device based on SLG, the prerequisite is having a much larger surface-incident optical absorption in SLG before Fermi level tuning. This way, the 2D photonic surface will demonstrate a notable increase in reflectance or transmittance upon gating when the SLG absorption is decreased to ~0. Optical absorption enhancement with broad optical bandwidth is highly desirable to best utilize the broad optical absorption spectrum of SLG. Meanwhile, tunable SLG photonic devices should have a capacitor-like structure, with an insulator layer between SLG and another conductor layer to modify the carrier density in SLG by charging/discharging the capacitor. For consumer applications, these devices must also be scalable to large area at low cost.

Numerous approaches have been investigated to increase the free-space optical absorption of SLG, including plasmonics [12, 13] and high refractive index dielectric nanophotonic structures [14, 15]. Most of them require nanolithography [13-16] and/or noble metal deposition [12, 13], which are hardly scalable to large-area devices. In addition, the plasmonic resonance peak is relatively narrow in spectrum, unless further modified by increasing damping [17] or incorporating various resonator sizes [18], which are even more complicated. Self-assembly of noble metal nanostructures on top of SLG using conventional vacuum evaporation followed by thermal annealing also tends to damage the crystal lattice of SLG according to the report of Liu et al. [12].

In this Paper, we introduce an optical slot-antenna-coupled cavity (SAC) framework that can simultaneously enhance SLG optical absorption by up to 20x and potentially enable electrical gating to tune its optical spectrum. Antennas were first utilized in radio wave regime to concentrate electromagnetic energy within a small volume $<<\lambda^3$ for effective radio detection [19]. Similarly, optical antennas are designed to efficiently convert free-space optical radiation energy into localized energy and vice versa at deep sub-wavelength scale, typically in the visible and near infrared (NIR) spectral regimes [20]. To achieve efficient and scalable optical antennas without complicated nanolithography, we utilize self-assembled, close-packed ultrahigh refractive index semimetal Sn nanodots (n~8-10 in NIR regime) separated by ~10 nm nanogaps, concentrating the incident light into the nanogaps similar to the principles of slot waveguides [21, 22]. These self-assembled optical slot-antennas are further coupled to an optical cavity to form the optical SAC framework, analogous to cavity-backed slot antennas in radio wave and microwave regimes [23]. The optical slot-antennas effectively funnel the incident light into the

underlying SLG regions with >100x electromagnetic near-field enhancement, and scatter the light into oblique angles for coupling into the laterally propagating slab modes in the cavity to further increase SLG absorption. Therefore, this optical SAC framework goes beyond conventional optical antennas or Fabry-Perot cavities by synergistically integrating near-field enhancement with optical resonances. Actually, the acronym of "SAC" also refers to the fact that light is funneled and trapped into the cavity, analogous to the way that ink is sucked into a fountain pen sac. As an example, we demonstrate that SLG in a Sn nanodot/SLG/100 nm SiO_2/Al optical SAC shows a dramatic optical absorption enhancement from 1-2% to 10-25% at λ=600-1900 nm, as confirmed by up to 120× enhancement in Raman scattering and significantly increased photo-conductance in SLG. The optical SAC also forms a semimetal/dielectric/metal capacitor to allow potential electrical gating. Compared to very recent investigations on slot-cavity interactions in guided waves [24, 25], our optical SAC framework extends such interactions into free space towards tunable 2D photonic surfaces.

2. Results and Discussion

2.1 Design Concept of Optical SAC

Figure 1a is a schematic illustration of our optical SAC framework design, based on an example of Sn nanodots/SLG/100 nm SiO_2/Al structure. Semimetals, such as Sn, Bi, and Sb, have a small overlap between the bottom of the conduction band and the top of the valence band in their band structures [26]. Hence the Fermi level can intercept with both the conduction band and the valence band. The inter-band transitions coming from this feature of quantum states occupation lead to ultrahigh refractive indices of semimetals in visible and NIR light regimes, as theoretically investigated in other literature [27]. For example, Sn has a much higher refractive index (n~8-10) [10, 27] than conventional high index dielectric materials (typically n≤4) [28] in the NIR spectrum.

Utilizing this novel optical property as well as the concept of slot waveguide [21, 22] and slot antennas, self-assembled Sn nanodots separated by ~10 nm nanogaps have been identified as a good candidate to build near-field slot-antennas for effectively manipulating light-SLG interactions [10]. Due to the continuity of the electric displacement at the boundary between two media, the magnitude of the electric field at the nanogaps/slots (n=1) between two high refractive index Sn nanodots (n~8-10) is greatly enhanced, similar to the case of slot waveguides. Therefore, the optical power can be strongly concentrated into the nanogaps for highly effective photon management. To further enhance SLG optical absorption and simultaneously enable electrical gating to tune its Fermi level, the SLG is inserted into a Sn nanodots/SLG/dielectric/metal optical SAC framework. Since SLG is also a 2D Dirac semimetal at room temperature [29], this Sn/SLG/SiO_2/Al optical SAC also constitutes a semimetal-insulator-metal parallel-plate capacitor structure towards potential electrical gating. The nanogaps between the ultrahigh refractive index Sn nanodots effectively concentrate and funnel the incident light into the underlying SLG regions with >100x electromagnetic near-field enhancement, and scatter the incident light into oblique angles. Reflection by the backside Al layer and scattering by the frontside Sn nanodots couple the light into laterally propagating slab modes in the optical SAC to drastically enhance the SLG absorption, ~10x more effective than a simple back-reflector alone. The SiO_2 layer deposited by plasma-enhanced chemical vapor deposition (PECVD) also introduces atomic hydrogen to significantly reduce the surface recombination at the Sn/SLG and SLG/SiO_2 interfaces compared to our previous work [10], as evidenced by a complete transfer of SLG optical absorption enhancement to the same amount of photocurrent multiplication to be discussed in Section 2.5. Therefore, this optical SAC framework greatly enhances SLG absorption and effectively improves the interface quality towards electrical gating at the same time.

Furthermore, the enhanced SLG absorption spectrum can be controlled by the insulator thickness, offering flexibility for optical design. For example, as will be shown in Section 2.6, SLG embedded in this optical SAC framework with a 150 nm-thick SiO_2 layer displays a distinctive red color in contrast to its surrounding regions without SLG on the same

sample under white light illumination, opening a potential path towards spectrally tunable reflectors by gating 2D photonic surfaces. This facile bottom-up nanofabrication process is also scalable to large-area 2D devices.

2.2 Enhanced Absorption Spectra of SLG in the Optical SAC

Figure 1b compares the photos of our samples with and without photonic structures. The lower panel corresponds to a reference pristine SLG transferred onto a fused quartz substrate without any photonic structures. The SLG, located in the middle of the sample and indicated by the white rectangle, is nearly transparent in the photo. This is because it only absorbs ~1.4% of the incident light, as mentioned earlier [10]. The middle panel corresponds to an SLG/SiO_2/Al optical cavity sample without Sn nanodots (i.e. without optical slot-antenna). On the same sample, there is a clear optical contrast between the middle area with SLG and the surrounding area without SLG. The darker color of the area with SLG indicates higher optical absorption in the visible spectrum regime compared to the surrounding area. Since the only difference between them is the existence of SLG, we can conclude that the enhanced absorption comes from SLG. Note that the region with SLG is also clearly darker than the SLG/quartz reference sample (lower panel of **Figure 1b**) due to absorption enhancement. The upper panel shows a photo of the ultrahigh refractive index Sn nanodots/SLG/SiO_2/Al optical SAC sample. Compared to the SLG/SiO_2/Al cavity structure (middle panel), the optical contrast between the regions with and without SLG is even higher and the SLG region appears much darker, indicating that the SLG absorption is further enhanced thanks to the coupling between the optical slot-antennas and the cavity.

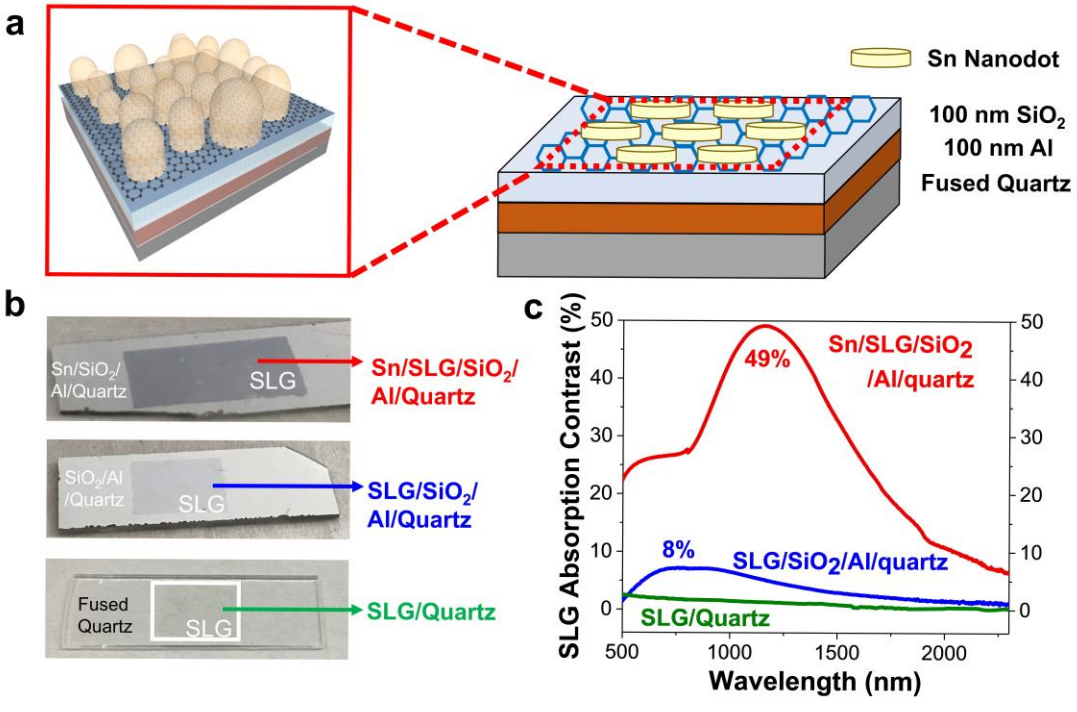

Figure 1 (a) A schematic illustration of the optical SAC framework. The 3D schematic figure on the left illustrates a zoomed-in view of the Sn nanodot/SLG region. **(b)** Photos of pristine SLG transferred on fused quartz substrate (**Lower panel**), the SLG/SiO_2/Al/quartz optical cavity sample (**Middle panel**), and the Sn nanodot/SLG/SiO_2/Al/quartz optical SAC sample (**Upper panel**). The SLG is in the middle of these samples. For the lower panel, the SLG region indicated by the white rectangular is nearly transparent. For the middle and upper panels, the SLG regions are darker than the surrounding regions on the same piece of sample due to the photon management effect introduced by the cavity or optical SAC, respectively. **(c)** Absorption contrast spectra induced by SLG on different samples, defined as the difference in absorption between the regions with and without SLG on the same sample. For the Sn/SLG/SiO_2/Al optical SAC, the absorption contrast is contributed by the enhanced SLG absorption as well as the morphological differences between the Sn nanodots deposited on SLG and on SiO_2, as will be discussed in **Figure 2** and **Figure S4**.

The observation above has been further quantified by measuring the optical absorption contrast spectra between the regions with and without SLG, as shown in **Figure 1c**. Transmittance (T) and reflectance (R) spectra are measured using a UV-VIS-NIR Spectro-photometer equipped with integrating sphere to capture both collimated and diffuse light [10]. The absorption (A) is obtained by A=1-T-R. Note that the optical absorption in the samples with Al coatings is simply A=1-R since the transmittance T=0 due to the opaqueness of the Al layer. For the same piece of sample with transferred SLG in the middle, the absorption contrast induced by SLG is defined as the difference in absorption between the regions with and without SLG (**Figure 1c**). That is, the absorption spectrum of the SLG/quartz region is compared to that of the blank quartz substrate region, the SLG/SiO_2/Al/quartz region to the SiO_2/Al/quartz region, and the Sn/SLG/SiO_2/Al/quartz region to the Sn/SiO_2/Al/quartz region, each pair being on the same sample as shown in **Figure S1**. For the SLG/quartz reference sample and the SLG/SiO_2/Al cavity sample, such an absorption contrast on the same sample can be considered as the net optical absorption from the SLG since there is no other difference between the middle and the surrounding regions. For the Sn nanodots/SLG/SiO_2/Al optical SAC sample, on the other hand, such contrast can be contributed by two factors: (1) enhanced absorption in SLG due to the photon management of the optical SAC framework. In this case, the ultrahigh refractive index Sn nanodots play a critical role in concentrating the incident light into the nanogaps between them, funneling the light into SLG, and coupling the light into the optical cavity. (2) enhanced absorption from the Sn nanodots on SLG due to their morphological differences from those on PECVD SiO_2. These factors will be discussed in more detail in the later text.

The optical absorption of SLG in the pristine SLG/quartz reference sample reaches up to 2.3% at λ~500 nm (i.e. the green curve in **Figure 1c**). Due to the p-type doping of SLG transferred to the fused quartz substrate, the absorption keeps decreasing as the wavelength increases, and it approaches zero at λ>2000 nm [10]. For the SLG/SiO_2/Al cavity structure, up to 8% absolute optical absorption from SLG is achieved at λ=700-900 nm, as shown by the blue curve in **Figure 1c**. Note that the maximal absorption enhancement (compared to the SLG/quartz reference) already reaches ~6x, much larger than 2x enhancement from a simple back-reflector. This result confirms that the SLG/SiO_2/Al cavity introduces multi-pass optical absorption in SLG. For the Sn/SLG/SiO_2/Al optical SAC sample, we observe an extremely high optical absorption contrast up to 49% between the regions with and without SLG, as the red curve shows in **Figure 1c**. In both cases, the SLG optical absorption contrast spectra cover an extremely broad spectral range from visible to IR (λ=500-2500 nm), demonstrating a great potential for broad-band surface-incident 2D photonic devices.

Due to the difference in surface energies between the PECVD SiO_2 and the SLG [30], we found that the Sn nanodots on SLG indeed showed some differences in morphology from those on SiO_2 in the same deposition process. This is characterized by scanning electron microscopy (SEM) images in **Figure S2**. Therefore, the very large absorption contrast (up to 49%) between the regions with and without SLG observed in the Sn/SLG/SiO_2/Al optical SAC sample (**Figures 1b** and **1c**) is not completely attributed to the enhanced absorption in SLG. To elucidate the photon management mechanism of the Sn nanodot/SLG/SiO_2/Al optical SAC and single out the enhanced absorption in SLG for comparison with that of the SLG/SiO_2/Al cavity, we performed wave optics modeling using COMSOL. We also compare the calculated SLG absorption data with experimental results of both Raman scattering enhancement and photo-conductance enhancement in SLG to verify the consistency.

2.3 Wave Optics Simulation and Photon Management Mechanisms of SLG in Optical SAC

The wave optics modeling results are summarized in **Figure 2**. For the SLG/SiO_2/Al cavity structure without Sn nanodots optical slot-antennas, **Figure 2a** shows that the calculated absorption spectrum largely agrees with the experimental data measured by UV-VIS-IR spectro-photometer (also shown previously in **Figure 1c**). Note that we used the optical conductance and refractive indices of intrinsic

SLG in the simulation, which leads to the slight deviation from the experimental data since the SLG transferred on SiO_2 is p-type [10]. **Figure 2b** further reveals that the enhanced SLG absorption is attributed to the optical field enhancement in SLG induced by the optical resonance and confinement in the SLG/SiO_2/Al cavity. The field enhancement factor in SLG, defined as $|E|^2/|E_0|^2$ where E and E_0 are the electric fields in SLG in the photonic structure and on quartz substrate, respectively, is slightly higher at λ=750 nm ($|E|^2/|E_0|^2$~3.07) than at λ=500 nm ($|E|^2/|E_0|^2$~2.55). Since optical absorption is proportional to $|E|^2$ [31], these field enhancement factors lead to ~7.1% absorption at 750 nm and 5.9% absorption at λ=500 nm from the SLG in the SLG/SiO_2/Al cavity structure, in reference to the absorption of pristine SLG on quartz in **Figure 1c**. Both numbers agree with the measured absorption spectrum (red line) in **Figure 2a**.

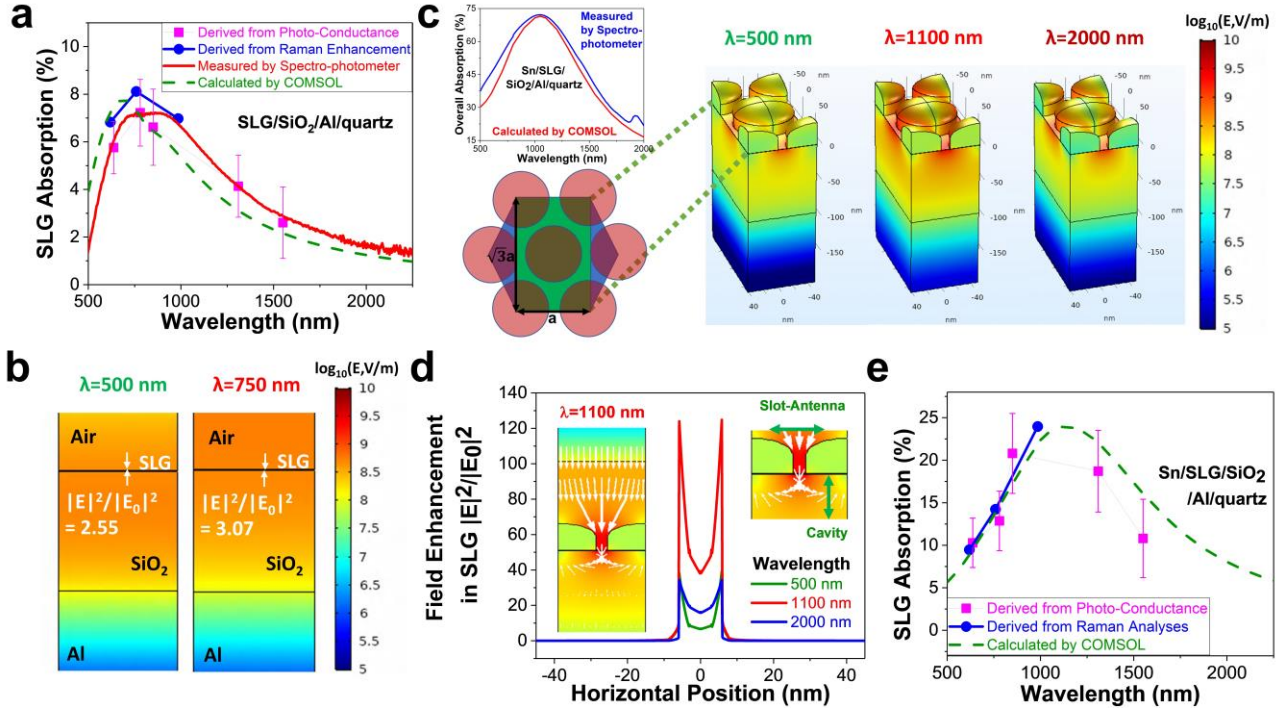

Figure 2 (a) Calculated (green line) vs. experimentally measured (red line) SLG absorption spectra from the SLG/SiO_2/Al/quartz cavity sample. The calculated data agree with the experimental results. The SLG absorption data derived from Raman peak enhancement (blue dots) and photo-conductance enhancement (magenta dots) are also shown in the figure. They correspond to the results and analyses from **Figures 3 & 4**, which will be discussed later. **(b)** The electric field distributions under optical excitation at λ=500 nm (**left panel**) and λ=750 nm (**right panel**) for the SLG/SiO_2/Al/quartz cavity. The unit of the electric field is V/m. The color bar is in log scale. **(c)** The electric field distributions (in 3D) under optical excitation at λ=500 nm (**left panel**), λ=1100 nm (**middle panel**), and λ=2000 nm (**right panel**) for the Sn nanodot/SLG/SiO_2/Al/quartz optical SAC sample. The unit of the electric field is V/m. The modeling is based on a close-packed hexagonal lattice of Sn nanodots, and the unit cell used in the simulation is schematically shown by the green-shaded region in the lower-left panel of (c) (top view, a=90 nm based on SEM and AFM analyses). The modeled overall absorption spectrum agrees very well with the experimentally measured one, as shown in the upper-left panel of (c). **(d)** shows the field enhancement ($|E|^2/|E_0|^2$) as a function of the horizontal position in the SLG layer of the Sn/SLG/SiO_2/Al/quartz optical SAC sample at λ=500 nm, 1100 nm and 2000 nm. The center of the gap between Sn nanodots correspond to x=0. The inset of (d) on the left side shows the corresponding field distribution and optical power flux at λ=1100 nm, using the same color scale as that of (b) and (c). The white arrows indicate the directions and magnitude (in logarithmic scale) of the optical power flux. Based on this analysis, the enhanced absorption in SLG is mainly attributed to (1) the optical field strongly concentrated to the nanogaps between the ultrahigh refractive index Sn nanodots and funneled into the underlying SLG regions; (2) coupling of incident light into optical SAC framework due to the scattering of Sn nanodots and back reflection of the Al layer. The inset of (d) on the right side schematically illustrates the orthogonal orientations of optical confinement inside the slot-antenna and the cavity. **(e)** Calculated SLG absorption spectra (green line) from the Sn/SLG/SiO_2/Al/quartz optical SAC sample compared to those derived from experimentally measured Raman peak enhancement (blue dots) and photo-conductance enhancement (magenta dots). The Raman and photo-conductance data correspond to the results and analyses in **Figure 3 & 4.**

For the Sn/SLG/SiO_2/Al optical SAC, based on the atomic force microscopy (AFM) analysis in **Figure S3** together with the SEM analysis in **Figure S2**, the pseudo-periodic Sn nanostructures are modelled as a close-packed periodic array of "cylinder + hemi-ellipsoid dome" structures [10]. Statistically, the heights of the cylinder and the dome are both 15 nm. The diameter of the cylinder is 78 ± 2 nm and the gap between the dots is 12 ± 2 nm (referring to **Figure S2** and **S3**). When the length scale of the ordering is much greater than the wavelength of interest, periodic approximation can be well applied in the optical simulation for pseudo-periodic photonic structures, as validated in previous literature [32, 33]. The actual thickness of the nominal 100 nm PECVD SiO_2 layer, functioning as the dielectric medium of the optical cavity, is characterized to be 95 ± 2 nm as shown in the cross-sectional SEM in **Figure S3**. A top view of the unit cell of the simulated structure is schematically shown by the green shaded region in the lower-left panel of **Figure 2c**. Using these parameters, the calculated overall absorption spectrum of the Sn/SLG/SiO_2/Al/quartz optical SAC sample agrees very well with the experimental results, as shown in the upper-left panel of **Figure 2c**. Due to the n-type compensation doping effect of the Sn nanostructures [10], the SLG in the Sn/SLG/SiO_2/Al optical SAC is nearly intrinsic, leading to a better agreement between the experimental data and the theoretical modeling utilizing the refractive indices of intrinsic SLG. The theoretical modeling also allows us to single out the absorption from the SLG in the Sn/SLG/SiO_2/Al framework, as shown by the dashed green curve in **Figure 2e**. The SLG optical absorption peaks at 24% at λ~1150 nm with an ultrabroad full width at half maximum (FWHM) of ~1000 nm from λ=700-1700 nm. This is an outstanding result for ultra-broadband photon management in SLG towards broad-spectrum electrical gating of 2D photonic surfaces. The mechanism of this broadband photon management effect will be discussed in the following paragraphs. The rest of the absorption contrast between the regions with and without SLG in the Sn/SLG/SiO_2/Al optical SAC sample, shown by the red curve in **Figure 1c,** is attributed to the morphological differences between the Sn nanostructures on SLG and on SiO_2, as detailed in **Figure S4**.

The right panel of **Figure 2c** further illustrates the three-dimensional (3D) optical field distribution when different wavelengths of independent light interact with the Sn/SLG/SiO_2/Al/quartz optical SAC. Firstly, the incident optical power is concentrated to the nanogaps between the Sn nanodots and funneled into the underlying SLG layer due to the ultrahigh refractive index of Sn nanostructures compared to that of the air gap, as discussed previously. Looking at the field enhancement profile in the SLG in **Figure 2d**, 50-130× local field enhancement $|E|^2/|E_0|^2$ can be achieved in the SLG region under the nanogaps between the Sn nanostructures at λ =1100 nm. Even though the electric field near the center of the Sn nanodots is compromised to some extent, we still obtain a dramatic overall absorption enhancement (proportional to $|E|^2/|E_0|^2$) in SLG (see **Figure 2e**) thanks to the strongly enhanced electromagnetic field in the nanogaps and the SLG regions underneath. This analyses further confirms the near-field photon management effect of the ultrahigh refractive index Sn nanodot optical slot-antennas.

Secondly, as the optical field is funneled through the nanogaps, it is scattered into oblique incidence angles (see the simulated optical power flow in the inset of **Figure 2d** and **Figure S5**). The front-side optical scattering by the Sn nanodots optical slot-antennas and the backside reflection by the Al layer synergistically couple the light into laterally propagating slab modes in the Sn/SLG/SiO_2/Al optical SAC to further elongate the optical path for SLG absorption enhancement, much more effective than the vertical cavity structure alone in **Figure 2a**.

Since the resonant wavelength is proportional to the effective optical path length in the cavity, the redshift of resonant absorption peak from λ~800 nm in **Figure 2a** to λ~1150 nm in **Figure 2e** suggests that the oblique scattering of Sn nanodots increases the optical path length, and hence the SLG absorption, by ~1.5x. Further considering that the peak absorption increases by ~3x from ~8% in the SLG/SiO_2/Al cavity to ~24% in the Sn nanodot/ SLG/SiO_2/Al optical SAC, we can also estimate that the optical slot-antennas contributed to another ~2x enhancement in SLG absorption via near-field enhancement. Therefore, near-field photon management and coupling to the lateral-propagation modes in the optical cavity contributed synergistically to SLG absorption enhancement in the optical SAC framework.

To verify the theoretically calculated SLG absorption in the optical SAC framework, we further performed experimental analyses of Raman scattering and photo-conductance enhancement in SLG, as summarized by the blue and magenta symbols in **Figure 2a and 2e**. These will be detailed in the next two sections.

2.4 Field Enhanced Raman Scattering Intensities of SLG Embed in Optical SAC Framework

Raman spectroscopy analyses are performed to experimentally verify the SLG absorption in the Sn/SLG/SiO_2/Al optical SAC framework modeled in **Figure 2** and to examine the quality of SLG upon Sn nanodots deposition. Raman scattering intensity is approximately proportional to $|E|^4$ [34] while optical absorption is proportional to $|E|^2$, where E is the electric field of the optical excitation wave. Therefore, the field enhancement and optical absorption enhancement in SLG can be derived from the corresponding Raman peak intensity enhancement using the equation below [10]:

$$\frac{I_{G+2D}(SLG\ in\ optical\ SAC\ Framework)}{I_{G+2D}(SLG)} = \frac{|E|^4}{|E_0|^4} \cdot T_{Raman} \qquad (1)$$

Here, $I_{G+2D}(SLG\ in\ optical\ SAC\ Framework)$ and $I_{G+2D}(SLG)$ refer to the integrated Raman peak intensities of SLG with and without optical SAC framework, respectively; E and E_0 are the electric fields in SLG with and without optical SAC framework, respectively. G band and 2D band are two major characteristics of SLG in Raman spectroscopy used for integrated Raman peak intensity calculations. Because the Raman-scattered photons generated in the SLG region of optical SAC framework have to transmit through any layer on the top of the SLG before getting collected by the Raman spectrometer, a term T_{Raman} is multiplied to represent the transmittance of the Raman-scattered photons. For the SLG/SiO_2/Al cavity structure, T_{Raman} is close to 1 since the incident light of Raman spectroscopy system interacts with SLG directly. For the Sn/SLG/SiO_2/Al optical SAC framework, T_{Raman} is reduced due to the scattering and absorption of the Sn nanodots on top of SLG. Since the transmittance loss of the quartz substrate is negligible, we can well approximate T_{Raman} by the transmittance of Sn nanodots/quartz at the corresponding Raman scattering wavelengths. Using the experimentally measured morphological parameters of Sn nanostructures on the top of SLG/SiO_2/Al/quartz (as discussed in previous text) and COMSOL Multiphysics software Wave Optics module, we calculated the transmittance spectrum of Sn nanostructures on quartz, as shown in **Figure S6**.

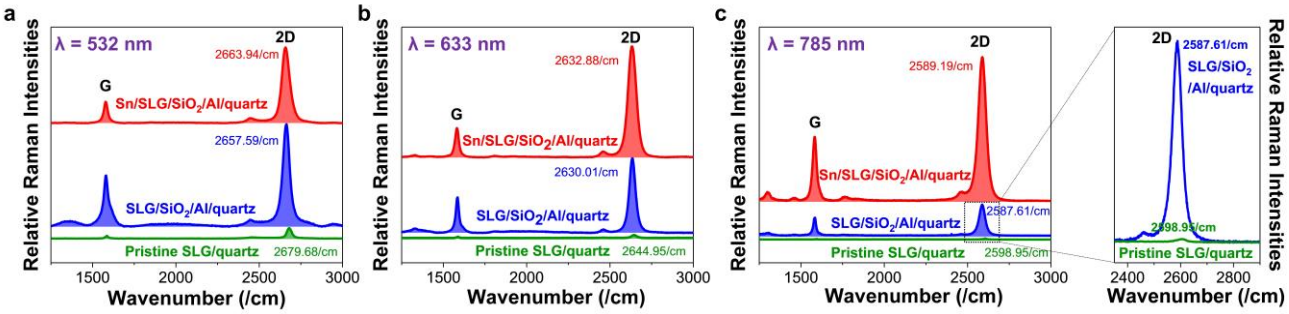

Figure 3 Raman spectra of SLG with and without photonic structures at excitation wavelengths of **(a)** 532 nm; **(b)** 633 nm; and **(c)** 785 nm. The red, blue, and green shaded areas correspond to the integrated Raman intensities of G and 2D bands in Sn/SLG/SiO_2/Al/quartz optical SAC, SLG/SiO_2/Al/quartz cavity, and reference pristine SLG/quartz samples, respectively. Quantitative analyses of the field-enhanced Raman peak intensities are summarized in **Table 1** and **Table 2**. A zoom-in of (c) is also provided to demonstrate the dramatically enhanced Raman peak due to photon management of SLG.

Figures 3a-c are the Raman spectra of pristine SLG/quartz, SLG/SiO_2/Al/quartz cavity, and Sn/SLG/SiO_2/Al/quartz optical SAC samples under the excitation wavelengths of 532 nm, 633 nm, and 785 nm, respectively. The redshift of 2D band from pristine SLG/quartz sample to SLG/SiO_2/Al/quartz and Sn/SLG/SiO_2/Al/quartz cavity samples indicates an n-type compensation doping effect [10]. This is beneficial for SLG absorption at longer wavelengths since the SLG becomes more intrinsic with the Fermi level close to the Dirac point. The G band and 2D band Raman peaks from the SLG region of the optical SAC samples increase by 1-2 orders of magnitude compared to those from the SLG/quartz reference, confirming the strong field enhancement and optical absorption enhancement in SLG due to the photon management effect. The Raman peaks from the SLG region of Sn/SLG/SiO_2/Al optical SAC framework samples (i.e. red shaded region) are also significantly stronger than those of the SLG/SiO_2/Al structure samples (i.e. blue shaded region) under 633 and 785 nm excitation, which is consistent with our previous analyses on optical absorption in SLG. This result confirms that the SLG photon management does contribute to the optical absorption contrast in **Figure 1c**.

Table 1 Summary of the integrated Raman peak intensity ratios I_{G+2D} (SLG in SLG/SiO_2/Al cavity)/ I_{G+2D} (SLG on quartz) at different excitation wavelengths, the field enhancement ratios $|E|^2/|E_0|^2$ in SLG derived from Eq. 1, and the derived SLG absorption in the SLG/SiO_2/Al cavity structure (which are also plotted in **Figure 2a** as the blue dots). Here I_{G+2D} is calculated as the integrated intensity of the G band and the 2D bands of SLG.

Excitation Wavelength	Raman Intensity Ratio $\frac{I_{G+2D}(SLG\ in\ SLG/SiO_2/Al\ cavity)}{I_{G+2D}(SLG\ on\ quartz)}$	Field Enhancement $\lvert E\rvert^2/\lvert E_0\rvert^2$	Derived SLG Absorption in SLG/SiO_2/Al Cavity Structure
532 nm	8.65	2.94	6.91%
633 nm	16.56	4.07	8.22%
785 nm	16.64	4.08	7.18%

Table 2 Summary of the integrated Raman peak intensity ratios I_{G+2D} (SLG in Sn/SLG/SiO_2/Al optical SAC framework)/ I_{G+2D} (SLG on quartz) at different excitation wavelengths, the corresponding transmittance of Raman-scattered photons through the Sn/SLG nanostructures (T_{Raman}), the field enhancement ratios $|E|^2/|E_0|^2$ in SLG derived from Eq. 1, and the derived SLG absorption in the Sn/SLG/SiO_2/Al optical SAC framework (which are also plotted in **Figure 2e** as the blue dots). Here the I_{G+2D} is calculated as the integrated intensity of the G band and the 2D band of SLG.

Excitation Wavelength	Raman Intensity Ratio $\frac{I_{G+2D}(SLG\ in\ Optical\ SAC)}{I_{G+2D}(SLG\ on\ quartz)}$	Transmittance of Raman-Scattered Photons T_{Raman}	Field Enhancement $\lvert E\rvert^2/\lvert E_0\rvert^2$	Derived SLG Absorption in Optical SAC Framework
532 nm	8.15	0.46	4.21	9.91%
633 nm	29.16	0.59	7.03	14.22%
785 nm	119.86	0.70	13.09	23.03%

The field enhancement $|E|^2/|E_0|^2$ is quantitatively derived using Equation (1) and the transmittance of the Sn/quartz sample in **Figure S6** at excitation wavelengths of λ=532, 633, and 785 nm. **Table 1** shows the field enhancement in SLG from the SLG/SiO_2/Al cavity sample compared to the pristine SLG/quartz sample, as derived from the Raman spectra. The SLG absorption derived from Raman scattering enhancement is also shown in **Table 1** and **Figure 2a** (the blue dots). The results are largely consistent with the absorption enhancement experimentally measured (i.e. the red curve) and theoretically calculated (i.e. the dashed green curve) in **Figure 2a**. **Table 2** further shows the SLG field enhancement in the Sn/SLG/SiO_2/Al optical SAC sample compared to the pristine SLG/quartz sample. The SLG absorption derived from the Raman peak enhancement of the Sn/SLG/SiO_2/Al optical SAC framework is also shown by the blue dots in **Figure 2e**. Again, the results agree very well with the SLG absorption singled out from the Sn/SLG/SiO_2/Al optical SAC sample (i.e. the dashed green curve in **Figure 2e**) based on wave optics modeling. These results confirm our theoretical model and further support the highly effective photon management in SLG by utilizing optical SAC framework.

2.5 Photo-Conductance Enhancement of SLG Embed in Optical SAC Framework

For practical applications in gate-tunable 2D photonic surfaces, it is important to test whether such a significantly enhanced optical absorption in SLG can be effectively transferred to the corresponding increase in photo-conductance. As discussed in Section 2.1, the complete transfer of optical absorption enhancement to photo-current multiplication is an indication of low surface recombination rate at the Sn/SLG and SLG/SiO_2 interfaces, a prerequisite for electrical gating. **Figure 4a** is a schematic illustration of our experimental setup, similar to what we reported previously [10]. A photo of our photo-conductor device is shown in the inset of **Figure S7**. The incident laser beams (~1-4 mW) at λ=637 nm, 780 nm, 850 nm, 1310 nm, and 1550 nm are modulated at >300 Hz by a function generator – a frequency high enough to minimize any laser induced thermal effect. The distance between the electrodes is approximately 1 cm, and the laser beam is incident within the SLG region. The electrical current and light modulating

frequency signals are coupled into a lock-in amplifier for more precise photocurrent measurement, i.e. only the photocurrent at the modulation frequency is amplified and recorded.

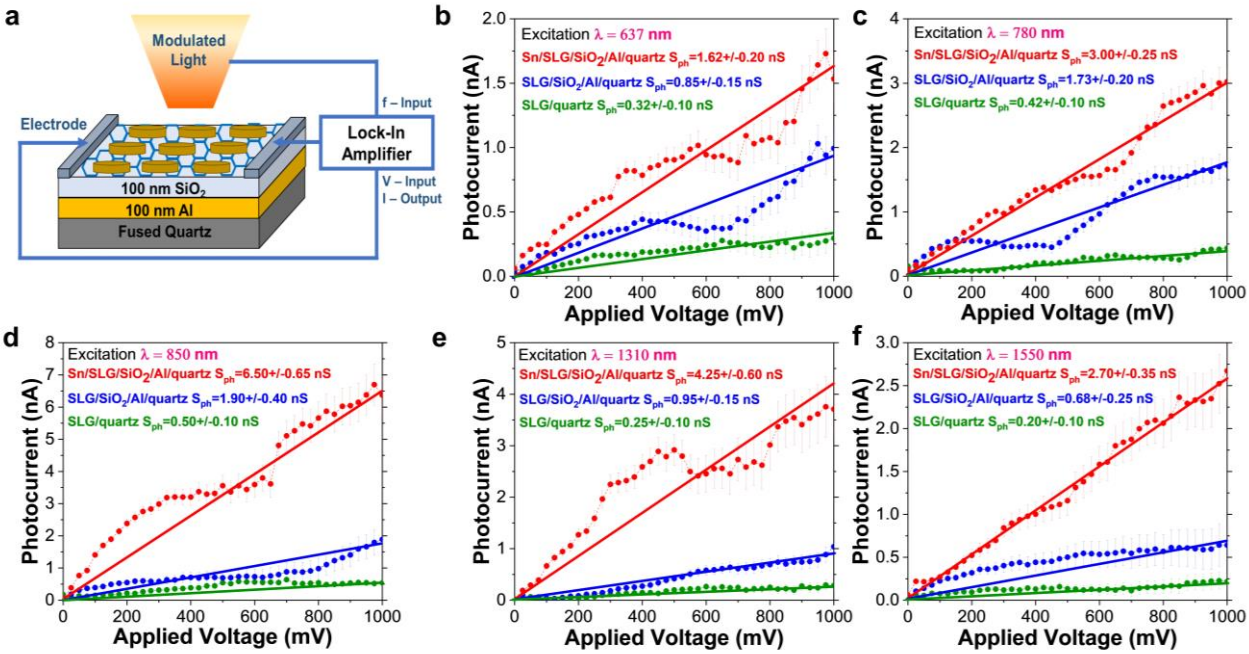

Figure 4 (a) Schematic experimental setup of the photocurrent measurement using a lock-in approach by modulating the laser diodes 300 Hz. Only the photocurrent, i.e. the change in current between the on and off state of the modulation, is amplified and recorded by the lock-in amplifier. Comparison of photocurrent vs. applied voltage for Sn/SLG/SiO_2/Al/quartz, SLG/SiO_2/Al/quartz, and pristine SLG/quartz samples are shown under different excitation wavelengths in: **(b)** at λ= 637 nm; **(c)** at λ= 780 nm; **(d)** at λ= 850 nm; **(e)** at λ= 1310 nm; **(f)** at λ= 1550 nm.

The I-V characteristics of these large area devices without illumination largely show an ohmic behavior, as indicated in **Figure S7**. The photocurrent measurement results are shown in **Figures 4b-f.** Considering 1-4 mW incident optical power, the measured responsivity is on the order of μA/W, comparably to a recent study on surface plasmon enhanced, micron-scale SLG photodetectors fabricated by e-beam lithography [35]. Advantageously, our self-assembly approach enables orders of magnitude larger device area (~cm^2 vs. tens of μm^2). The deviation from linearity in **Figures 4b-f** for photo-conductance measurements are mainly due to two reasons: (1) A much larger dark current in mA scale compared to the photocurrent in nA scale, which leads to the noises in **Figures 4b-f**. The error bars in photocurrent reflect the standard deviation in multiple scans. (2) For the optical cavity and optical SAC structures, the Al layer under SiO_2 acts as a common metal gate. When a voltage is applied between the two electrodes on SLG, the Fermi level/effective doping of SLG is actually changing gradually in the region between the two electrodes [36]. Furthermore, the Gaussian beam profiles of the incident lasers induce non-uniform distribution of photo-generated carriers and possibly Seebeck effect in SLG [36]. For the optical SAC sample, the size distribution of Sn nanodots also induces non-uniform compensation doping of SLG. These factors all lead to deviation from linearity in the dark I-V and photocurrent, as has been analyzed theoretically [37] and reported experimentally [36] in previous literature. On the other hand, despite of these non-idealities, a linear fit to the photo-conductance can still give us a good evaluation of SLG optical absorption enhancement. Looking at the measured photocurrents and photo-conductivities in **Figures 4b-f**, the SLG/SiO_2/Al cavity structure shows 2.7x, 4.1x, 3.8x, 3.8x, and 3.4x higher photo-conductance at λ=637 nm, 780 nm, 850 nm, 1310 nm, and 1550 nm than the reference pristine SLG/quartz sample, respectively. By comparison, the Sn/SLG/SiO_2/Al optical SAC sample shows 5.1x, 7.1x, 13.0x, 17.0x, and 13.5x higher photo-conductance at λ=637 nm, 780 nm, 850 nm, 1310 nm, and 1550 nm than the pristine SLG/quartz sample, respectively. Within the error ranges, these all match very well with the calculated SLG absorption spectra in **Figures 2a** and **2e**. This result again proves the highly efficient, ultra-broad-band photon management capability of the ultrahigh refractive index optical SAC framework. It also demonstrates that the optical absorption enhancement in SLG

directly transfers to the same amount of photo-conductance enhancement in these optical SAC samples, thanks to the diffusion of atomic hydrogen from PECVD SiO_2 through SLG to help passivate both the Sn/SLG and SLG/SiO_2 interfaces [38]. This interfacial passivation effectively overcomes the detrimental surface recombination issue at the Sn/SLG interface found in our previous work [10], which led to a lower photo-conductance enhancement than the optical absorption enhancement in SLG. This finding also provides a feasible approach to better passivate the interfaces of 2D photonic devices towards gate-tunable 2D photonic surfaces.

2.6 Spectral Tunability of Optical SAC Framework by Insulator Thickness

With the Optical SAC framework, not only the peak absorption of SLG is further enhanced from ~15% in our previous work [10] to ~25%, but the absorption enhancement spectrum can be effectively tuned by engineering the thickness of the insulating layer. To demonstrate it, we take another example of optical SAC framework, Sn/SLG/150 nm SiO_2/Al structure, as presented in **Figure 5**. For the SLG/150 nm SiO_2/Al cavity sample (i.e. without Sn nanodots), the SLG absorption peak position is notably redshifted into the IR regime compared to the cavity with 100 nm-thick SiO_2 layer presented previously (see **Figure 5a**), and the peak absorption is slightly increased to ~8.5%. Due to this redshift, the SLG absorption now shows a valley in the visible regime. Therefore, the corresponding photo in the visible spectrum shows little contrast between the regions with and without SLG (see the inset in upper right part of **Figure 5a**). For the Sn/SLG/150 nm SiO_2/Al optical SAC sample, the SLG absorption is singled out using the same method described earlier in the case of Sn/SLG/100 nm SiO_2/Al optical SAC framework, i.e. via wave optics modelling that matches the experimentally measured overall absorption spectra. A detailed breakdown of the optical absorption contributed by SLG, Sn, and Al in the sample with 150 nm SiO_2 is shown in **Figure S8**. With the ultrahigh refractive index Sn nanodots slot-antenna to provide strong field enhancement in SLG, **Figure 5b** shows that the optical absorption of SLG in the Sn/SLG/150 nm SiO_2/Al optical SAC framework is increased to >20% in a very broad IR spectral range of λ=1300-1900 nm compared to the cavity structure alone shown in **Figure 5a**. The absorption spectrum is also redshifted compared to their counterpart incorporating 100 nm-thick SiO_2 (**Figure 5b**), with an even broader FWHM of 1500 nm (λ=1000-2500 nm) vs. 1000 nm. Interestingly, the SLG region of the optical SAC sample with 150 nm thick SiO_2 also shows a higher order resonant absorption peak in the blue/green/yellow spectral regime at λ=400-600 nm, leading to a much smaller reflectance at λ < 600 nm (**Figure 5c**). Therefore, the region with SLG mostly reflects red light at λ>600 nm, demonstrating a vivid red color compared to its surrounding area without SLG (see the inset on the upper right part of **Figure 5b**). Such an effective spectral tunability of SLG absorption enables better optical performance of 2D photonic devices in a targeted optical band.

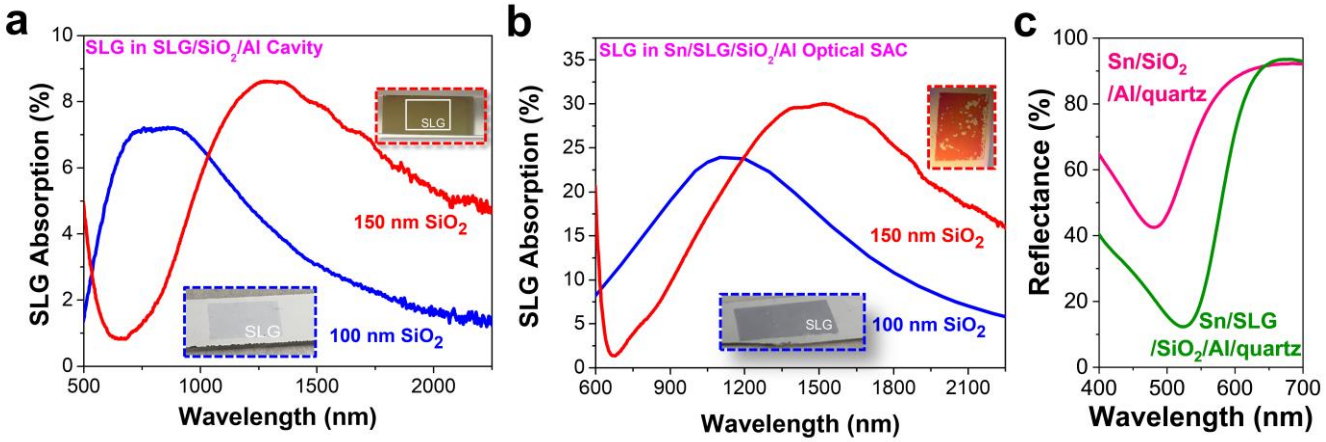

Figure 5 (a) SLG absorption spectra in SLG/SiO_2/Al optical cavities with 100 nm (blue line) and 150 nm-thick (red line) SiO_2 layers. The insets show the photos of the corresponding samples. **(b)** SLG absorption spectra in Sn/SLG/SiO_2/Al optical SAC framework with 100 nm (blue line) and 150 nm-thick (red line) SiO_2 layers. The insets show the photos of the corresponding samples. (c) Reflectance spectra of the Sn/SLG/150 nm SiO_2/Al cavity region (green line) and the surrounding Sn/150 nm SiO_2/Al region (magenta line), corresponding to the photo enclosed by the dashed red box in **Figure 5b**. The region with SLG demonstrates a low reflectance in the blue/green/yellow spectra at λ =400-600 nm and high reflectance in the red spectrum at λ>600 nm, leading to a vivid red color under white light illumination.

More importantly, compared with our previous report in Ref. [10], the capacitor-like optical SAC framework enables electrical gating of the SLG Fermi level and photon management at the same time. The position of SLG Fermi level E_F (in reference to the Dirac point) has a strong impact on its optical transition since any inter-band transition at photon energies $h\nu<2E_F$ is forbidden [6]. Therefore, the significantly enhanced SLG absorption over both visible and NIR regimes and the gating capability through our optical SAC framework potentially allows appreciable changes in the reflectance of the device via gate-variable optical transition in SLG. Considering the vivid red color of the SLG region in the Sn/SLG/150 nm SiO_2/Al optical SAC sample under white illumination, as shown in **Figures 5b** and **5c**, gate-tuning the optical transition of SLG could potentially modify the color appearance of the whole structure, thereby taking a step towards large-area 2D consumer devices such as spectral reflectors, band-pass filters, and low-power optical switches to substitute their MEMS counterparts.

3. Conclusion

In conclusion, to simultaneously enhance the optical absorption of SLG and potentially enable its electrical gating for tunable 2D photonic surfaces, we have demonstrated a highly effective and broadband optical SAC framework using an ultrahigh refractive index semimetal/SLG/insulator/metal structure. This framework synergistically integrates near-field enhancement induced by ultrahigh refractive index semimetal slot-antennas with broadband resonances in visible and infrared regimes, ~3x more effective than a vertical cavity structure alone. As an example of the optical SAC framework, a Sn nanodots/SLG/SiO_2/Al stack takes advantages of the unique ultrahigh refractive indices of semimetal Sn, effectively concentrating and funneling the incident light from free-space into the SLG region through the nanogaps between the self-assembled, closely packed Sn nanodots. Light is further scattered and coupled into the slab modes of optical SAC framework by the reflection of the backside Al layer. Utilizing this novel optical SAC framework, we achieve a peak SLG absorption of ~25% with a spectral FWHM as broad as 1500 nm. The optical absorption is enhanced by 5-20x compared to pristine SLG transferred onto quartz substrate in an ultra-broad spectral range of 500-2500 nm, covering the entire visible and near IR regimes. The strongly enhanced, broad-band SLG absorption in optical SAC framework has also been confirmed by field-enhanced Raman scattering (by 1-2 orders of magnitude) and significantly increased photo-conductance of SLG at multiple wavelengths, which is also spectrally tunable by engineering the thickness of the dielectric layer. Moreover, optical SAC framework also serves as a parallel-plate capacitor towards SLG-based gate-tunable 2D photonic surfaces for tunable visible and NIR reflectors/filters/attenuators, as well as optical switches. The fabrication of optical SAC framework samples based on deposition and self-assembly is facile and scalable to large area, bringing a great advantage to industrial manufacturing.

4. Methods

4.1 Preparation of Self-Assembled Pseudo-Periodic Sn Nanodots with Ultrahigh Refractive Index

A Lab18 Physical Vapor Deposition (PVD) system manufactured by Kurt J. Lesker Company is used to prepare the self-assembled pseudo-periodic Sn nanostructures via thermal evaporation. The chamber's base vacuum is 5×10^{-8} Torr. Sn tablets (99.99%, Kurt J. Lesker) are used as the source material for evaporation. Key parameters include the nominal thickness of the Sn deposition as well as the deposition rates (typically ~0.12 Å/sec), which determine the morphology of the Sn nanostructures. The dewetting of Sn on various surfaces leads to the self-assembly of Sn nanodots, similar to the Stranski-Krastanov mechanism [39]. Other details have been reported in Ref. [10].

4.2 Preparation of SLG on Various Substrates

The SLG used in this study is fabricated by chemical vapor deposition (CVD) [40]. PMMA-assisted SLG transfer technique is used [41, 42]. The fabrication process is identical to what has been reported in Ref. [10].

4.3 PECVD Deposition of SiO_2 Thin Film

The PECVD deposition of SiO_2 thin film is implemented with a Plasmatherm 740 SLR at 500 mTorr, 200 °C, with reagents of 150 sccm 5% SiH_4 in He, 600 sccm of N_2O and 600 sccm of N_2.

4.4 E-Beam Deposition of Al Thin Film

AJA International ATC-E Electron Beam Evaporator System is used to deposit aluminum thin film. Al tablets (99.999%, Kurt J. Lesker, #EVMAL50QXHJ)

with a diameter of 1/4" and length of ½" were used as raw material. The base pressure before evaporation is lower than 1×10^{-6} Torr. During the evaporation, the deposition rate is maintained at 0.5 Å/s.

4.5 Morphological Characterization

FEI Scios 2 dual beam system Scanning Electron Microscope and AIST-NT SmartSPM 1000 Atomic Force Microscope are used to characterize the morphologies of Sn nanostructures, i.e. Figure S2 and Figure S3. For AFM analysis, tapping mode is used in all cases. Statistical analyses of the diameters of Sn nanostructures and the gaps were conducted by manually collecting 200 diameter/gap data points on the SEM and AFM images of each sample.

4.6 Optical Characterization

The transmittance and reflectance spectra are measured by a Jasco V-570 spectrometer equipped with a Jasco ISN-470 integrating sphere, scanned from λ=300 nm to 2500 nm.

Acknowledgements

This work has been sponsored by National Science Foundation under the collaborative research awards #1509272 and #1509197. We thank Dr. Christopher Levey from Thayer school of Engineering at Dartmouth College for helpful discussions. We greatly appreciate the advanced characterization instruments of the Electron Microscope Facility at Dartmouth College and the materials processing instruments of the Micro-System Technology Lab at MIT.

Electronic Supplementary Material: Supplementary material (further SEM, AFM, optical, electrical characterization and wave optics simulation analy)is available in the online version of this article at http://dx.doi.org/10.1007/10.1007/s12274-***-****-* (automatically inserted by the publisher) and is accessible free of charge

References

[1] Mueller, T.; Xia, F.; Avouris, P. Graphene Photo-detectors for High Speed Optical Communications. *Nat. Photonics* **2010**, *4(5)*, 297-301.

[2] Goossens, S.; Navickaite, G.; Monasterio, C.; Gupta, S.; Piqueras, J. J.; Pérez, R.; Burwell, G.; Nikitskiy, I.; Lasanta, T.; Galán, T.; Puma, E.; Centeno, A.; Pesquera, A.; Zurutuza, A.; Konstantatos, G.; Koppens, F. Broadband Image Sensor Array based on Graphene–CMOS Integration. *Nat. Photonics* **2017**, *11*, 366-371.

[3] Song, Y.; Li, X.; Mackin, C.; Zhang, X.; Fang, W.; Palacios, T.; Zhu H.; Kong, J. Role of Interfacial Oxide in High-Efficiency Graphene–Silicon Schottky Barrier Solar Cells. *Nano Lett.* **2015**, *15(3)*, 2104-2110.

[4] Geim, A. K.; Novoselov, K. S. The Rise of Graphene. *Nat. Mater.* **2007**, *6*, 183-191.

[5] Mak, K. F.; Ju, L.; Wang, F.; Heinz, T. F.; Optical Spectroscopy of Graphene: From the Far Infrared to the Ultraviolet. *Solid State Commun.* **2012**, *152(15)*, 1341-1349.

[6] Wang, F.; Zhang, Y.; Tian, C.; Girit, C.; Zettl, A.; Crommie, M.; Shen, Y. R. Gate-Variable Optical Transitions in Graphene. *Science* **2008**, *320*, 206-209.

[7] Liu, M.; Yin, X.; Ulin-Avila, E.; Geng, B.; Zentgraf, T.; Ju, L.; Wang F.; Zhang, X. A Graphene-based Broadband Optical Modulator. *Nature* **2011**, *474*, 64-67.

[8] Phare, C. T.; Lee, Y. D.; Cardenas J.; Lipson, M.; Graphene Electro-Optic Modulator with 30 GHz Bandwidth. *Nat. Photonics* **2015**, *9*, 511–514.

[9] Sorianello, V.; Midrio, M.; Contestabile, G.; Asselberghs, I.; Campenhout, J. V.; Huyghebaert, C.; Goykhman, I.; Ott, A. K.; Ferrari, A. C.; Romagnoli, M. Graphene–Silicon Phase Modulators with Gigahertz Bandwidth. *Nat. Photonics* **2018**, *12*, 40-44.

[10] Fu, S.; Wang, H.; Wang, X.; Song, Y.; Kong J.; Liu, J. Self-Assembled, Ultrahigh Refractive Index Pseudo-Periodic Sn Nanostructures for Broad-Band Infrared Photon Management in Single Layer Graphene. *ACS Photonics* **2019**, *6(1)*, 50-58.

[11] Nair, R. R.; Blake, P.; Grigorenko, A. N.; Novoselov, K. S.; Booth, T. J.; Stauber, T.; Peres, N. M. R.; Geim, A. K. Fine Structure Constant Defines Visual Transparency of Graphene. *Science* **2008**, *320(5881)*, 1308.

[12] Deng, B.; Guo, Q.; Li, C.; Wang, H.; Ling, X.; Farmer, D. B.; Han, S.; Kong, J.; Xia, F. Coupling-Enhanced Broadband Mid-Infrared Light Absorption in Graphene Plasmonic Nanostructures. *ACS Nano* **2016**, *10(12)*, 11172−11178

[13] Liu, Y.; Cheng, R.; Liao, L.; Zhou, H.; Bai, J.; Liu, G.; Liu, L.; Huang, Y.; Duan, X. Plasmon Resonance Enhanced Multicolour Photodetection by Graphene. *Nat. Commun.* **2011**, *2*, 579.

[14] Liu, J.; Liu, N.; Li, J.; Li, X. J.; Huang, J. Enhanced Absorption of Graphene with One-Dimensional Photonic Crystal. *Appl. Phys. Lett.* **2012**, *101*, No. 052104.

[15] Khaleque, A.; Hattori, H. T. Absorption Enhancement in Graphene Photonic Crystal Structures. *Appl. Opt.* **2016**, *55(11)*, 2936−2942.

[16] Ding, F.; Yang, Y.; Deshpande R. A.; Bozhevolnyi, S. I. A Review of Gap-Surface Plasmon Metasurfaces: Fundamentals and Applications. *Nanophotonics* **2018**, *7(6)*, 1129-1156.

[17] Lerme, J. Size Evolution of the Surface Plasmon Resonance Damping in Ag Nanoparticles: Confinement and Dielectric Effects. *J. Phys. Chem. C* **2011**, *115(29)*, 14098-14110.

[18] Juve, V.; Cardinal, M. F.; Lombardi, A.; Crut, A.; Maioli, P.; Perez-Juste, J.; Liz-Marzan, L. M.; Fatti, N. D.; Vallee, F. Size-Dependent Surface Plasmon Resonance Broadening in Nonspherical Nanoparticles: Single Gold Nanorods. *Nano Lett.* **2013**, *13(5)*, 2234-2240.

[19] Eggleston, M.S.; Messer, K., Zhang, L., Yablonovitch, E., and Wu, M. C. Optical antenna enhanced spontaneous emission. *Proc. Natl. Acad. Sci.* **2015**, *112 (6)*, 1704-1709; DOI: 10.1073/pnas.1423294112

[20] Bharadwaj, P; Deutsch, B.; Novotny L. Optical Antennas. *Adv. Opt. Photonics* **2009**, *1*, 438-483.

[21] Anderson, P. A.; Schmidt, B. S.; Lipson, M. High Confinement in Silicon Slot Waveguides with Sharp Bends.

Opt. Express **2006**, *14(20)*, 9197−9202
[22] Barrios, C. A.; Sanchez, B.; Gylfason, K. B.; Griol, A.; Sohlstr m, H.; Holgado, M.; Casquel, R. Demonstration of Slot Waveguide Structures on Silicon Nitride/Silicon Oxide Platform. *Opt. Express* **2007**, *15(11)*, 6846−6856.
[23] Luo, G. Q.; Hu, Z. F.; Li, W. J.; Zhang, X. H.; Sun, L. L; Zheng, J. F. Bandwidth-Enhanced Low-Profile Cavity-Backed Slot Antenna by Using Hybrid SIW Cavity Modes. ***IEEE*** *Trans. ANTENN. PROPAG.* **2012**, *60(4)*, 1698-1704 doi: 10.1109/TAP.2012.2186226.
[24] Cognée, K. G.; Doeleman, H. M.; Lalanne, P.; Koenderink, A. F. Cooperative Interactions between Nano-Antennas in a High-Q Cavity for Unidirectional Light Sources. *Light Sci. Appl.* **2019**, *8*, No. 115.
[25] Palstra, I. M.; Doeleman H. M.; Koenderink, A. F. Hybrid Cavity-Antenna Systems for Quantum Optics outside the Cryostat? *Nanophotonics* **2019**, *8(9),* 1513-1531.
[26] Burns, G. *Solid State Physics*, 1st ed; Academic Press, **1985**.
[27] Takeuchi, K. and Adachi, S. Optical Properties of β-Sn Films. *J. Appl. Phys.* **2009**, *105(7)*, No. 073520.
[28] Baranov, D. G.; Zuev, D. A.; Lepeshov, S. I.; Kotov, O. V.; Krasnok, A. E.; Evlyukhin, A. B.; Chichkov, B. N. All-dielectric Nanophotonics: The Quest for Better Materials and Fabrication Techniques. *Optica* **2017**, *4(7)*, 814−825.
[29] Young S. M.; Kane, C. L. Dirac Semimetals in Two Dimensions, *Phys. Rev. Lett.* **2015**, *115*, No. 126803.
[30] Kozbial, A.; Li, Z.; Conaway, C.; McGinley, R.; Dhingra, S.; Vahdat, V.; Zhou, F.; D'Urso, B.; Liu, H.; Li, L. Study on the Surface Energy of Graphene by Contact Angle Measurements. *Langmuir* **2014**, *30(28)*, 8598-8606.
[31] Hayt, W. H.; Buck, J. A. *Engineering Electromagnetics*, 6th ed. McGraw-Hill Series of Electrical and Computer Engineering, **2000**.
[32] Wang, Z.; Wang, X.; Liu, J. An Efficient Nanophotonic Hot Electron Solar-Blind UV Detector. *ACS Photonics* **2018**, *5(10)*, 3989−3995.
[33] Sheng, X.; Liu, J.; Kozinsky, I.; Agarwal, A. M.; Michel J.; Kimerling, L. C. Design and Non-Lithographic Fabrication of Light Trapping Structures for Thin Film Silicon Solar Cells. *Adv. Mater.* **2011**, *23(7)*, 843−847.
[34] Campion. A.; Kambhampati, P. Surface-Enhanced Raman Scattering. *Chem. Soc. Rev.* **1998**, *27*, 241−250.
[35] Wang, D.; Allcca, A.E.L.; Chung, T.; Kildishev, A. V.; Chen, Y. P.; Boltasseva, A.; Shalaev, V.M. Enhancing the graphene photocurrent using surface plasmons and a p-n junction. *Light Sci. Appl* . **2020**, *9*, 126. https://doi.org/10.1038/s41377-020-00344-1.
[36] Freitag, M.; Low, T.; Xia, F.; Avouris, P. Photoconductivity of biased graphene. *Nature Photon* **2013**, *7*, 53–59 (2013). https://doi.org/10.1038/nphoton.2012.314
[37] Singh, A.; Ghosh, S.; Agarwal, A. Nonlinear, anisotropic, and giant photoconductivity in intrinsic and doped graphene. *Phys. Rev. B* **2018**, *97*, 045402.
[38] Webera, J. R.; Dangling-Bond Defects and Hydrogen Passivation in Germanium. *Appl. Phys. Lett.* **2007**, *91*, No. 142101.
[39] Eisenmenger-Sittner, C.; Bangerta, H.; St ri, H.; Brenner, J.; Barnac, P. B. Stranski−Krastanov Growth of Sn on a Polycrystalline Al Film Surface Initiated by the Wetting of Al by Sn. *Surf. Sci.* **2001**, *489(1−3)*, 161−168.
[40] Reina, A.; Jia, X.; Ho, J.; Nezich, D.; Son, H.; Bulovic, V.; Dresselhaus, M. S.; Kong, J.; Large Area Few-Layer Graphene Films on Arbitrary Substrates by Chemical Vapor Deposition. Nano Lett. **2009**, *9(1)*, 30−35.
[41] Wang, H.; Leong, W. S.; Hu, F.; Ju, L.; Su, C.; Guo, Y.; Li, J.; Li, M.; Hu, A.; Kong, J.; Low-Temperature Copper Bonding Strategy with Graphene Interlayer. *ACS Nano* **2018**, *12(3)*, 2395−2402.
[42] Leong, W. S.; Wang, H.; Yeo, J.; Martin-Martinez, F. J.; Zubair, A.; Shen, P.; Mao, Y.; Palacios, T.; Buehler, M. J.; Hong, J.; Kong, J. Paraffin-Enabled Graphene Transfer. *Nature Comm.* **2019**, *10*, No. 867.

Electronic Supplementary Material

An Optical Slot-Antenna-Coupled Cavity (SAC) Framework towards Tunable Free-Space Graphene Photonic Surfaces

Sidan Fu,[1] Xiaoxin Wang,[1] Haozhe Wang,[2] Xiaoxue Gao,[1] Kurt Broderick,[2] Jing Kong,[2] ✉ and Jifeng Liu[1] ✉

1 Thayer school of Engineering, Dartmouth College, 14 Engineering Drive, Hanover, New Hampshire 03755, USA.

2 Department of Electrical Engineering and Computer Science, Massachusetts Institute of Technology, 77 Massachusetts Avenue, Cambridge, Massachusetts 02139, USA.

Supporting information to DOI 10.1007/s12274-****-****-* (automatically inserted by the publisher)

Address correspondence to Jifeng Liu, Jifeng.Liu@Dartmouth.edu; Jing Kong, jingkong@mit.edu.

1. **Comparison of Absorption Spectra between the Regions with and without Graphene on the Same Sample**

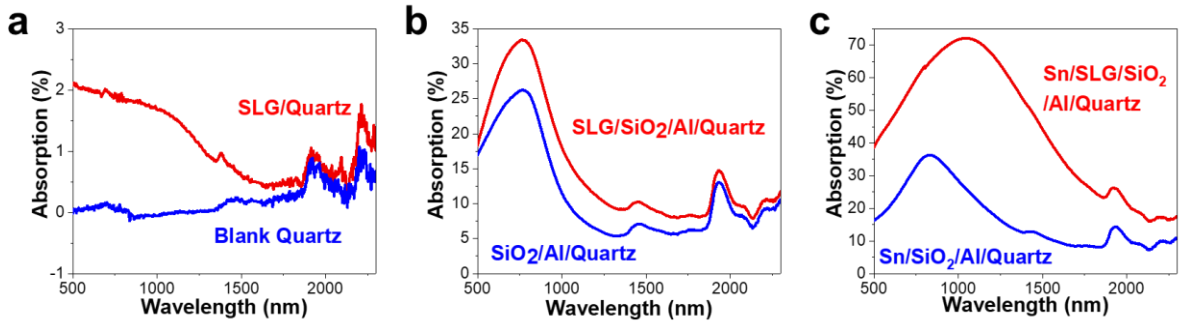

Figure S1 Comparison of absorption spectra on the same sample between the regions with and without SLG: **(a)** the SLG/quartz region (red line) vs. the blank quartz region (blue line); **(b)** the SLG/SiO_2/Al/quartz region (red line) vs. the SiO_2/Al/quartz region (blue line); **(c)** the Sn/SLG/SiO_2/Al/quartz region (red line) vs. the Sn/SiO_2/Al/quartz region (blue line).

2. Morphological Variation of Sn Nanostructures on Different Substrates

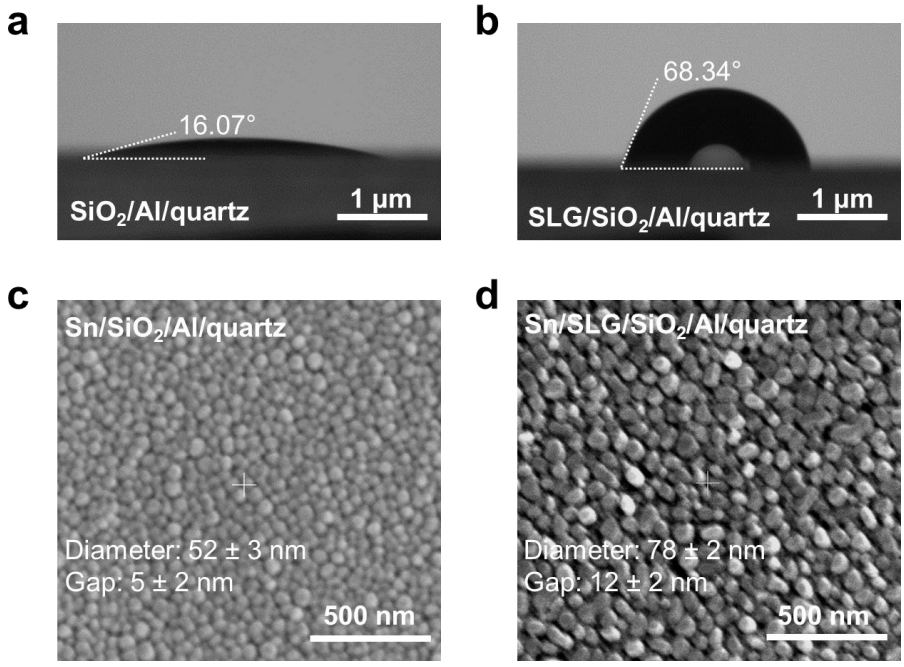

Figure S2 (a, b) Wetting angle measurement results of DI water droplet on PECVD SiO_2/Al/quartz and SLG/SiO_2/Al/quartz, respectively. DI water droplets on SLG/SiO_2/Al/quartz clearly show a much bigger contact angle than those on SiO_2/Al/quartz, which indicates a big difference in surface energies between them. (c, d) Scanning electron microscopy (SEM) images of Sn nanostructures on the two substrates shown in (a) and (b). Both the diameter of Sn nanodots and the gaps between them show a clear difference statistically.

3. Materials Characterization for Wave Optics Modeling in COMSOL

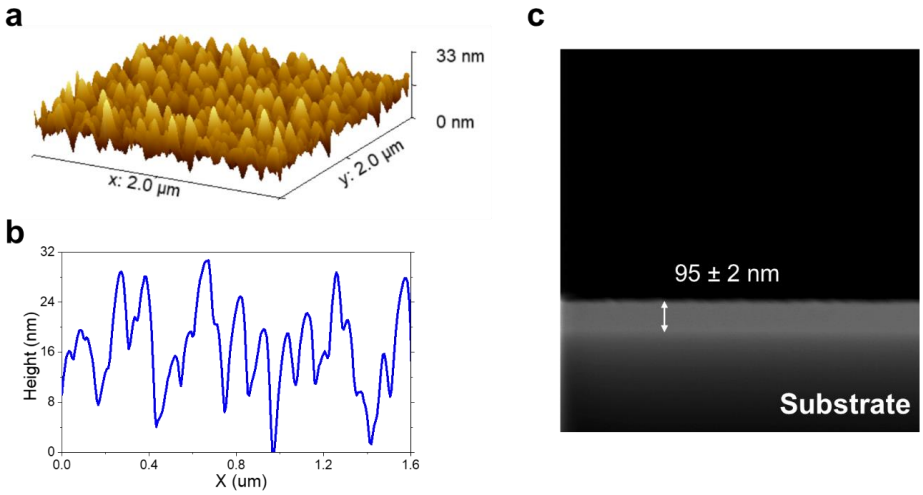

Figure S3 (a) Three-dimensional atomic force microscopy (AFM) image, and (b) cross-sectional profile of Sn nanostructures on SLG/100 nm SiO_2/Al/quartz. (c) Cross-sectional SEM photo of the nominally 100 nm-thick PECVD SiO_2 layer.

4. Contributors to the Optical Absorption Contrast in the Sn/SLG/100 nm SiO_2/Al Optical SAC Cavity Sample

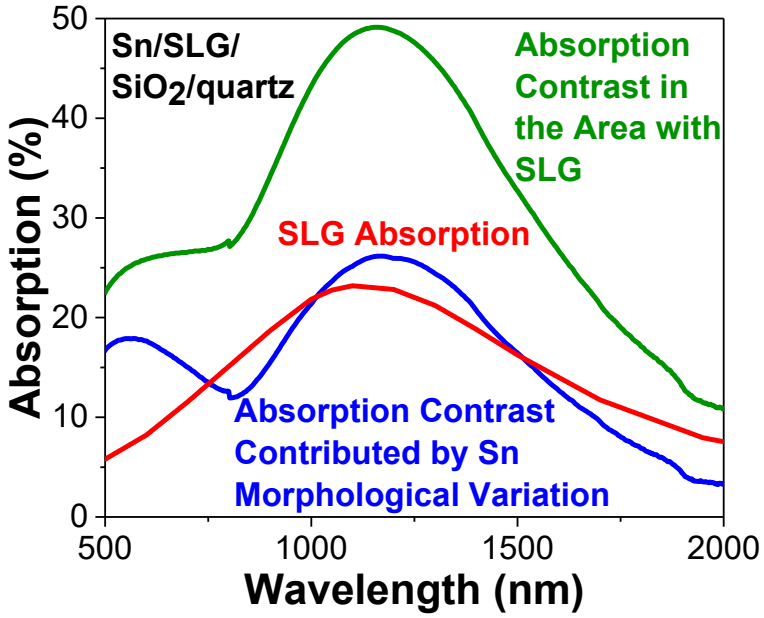

Figure S4 Experimentally measured optical absorption contrast between the areas with and without SLG (green line) in the Sn/SLG/100 nm SiO_2/Al Optical SAC cavity framework, contributed by both enhanced SLG absorption (red line; singled out using wave optics modeling) and the morphological differences between the Sn nanostructures deposited on SLG and on SiO_2 (blue line).

5. **Calculated Optical Power Flow through the Sn/SLG/100 nm SiO_2/Al Optical SAC Cavity Framework at Different Wavelengths**

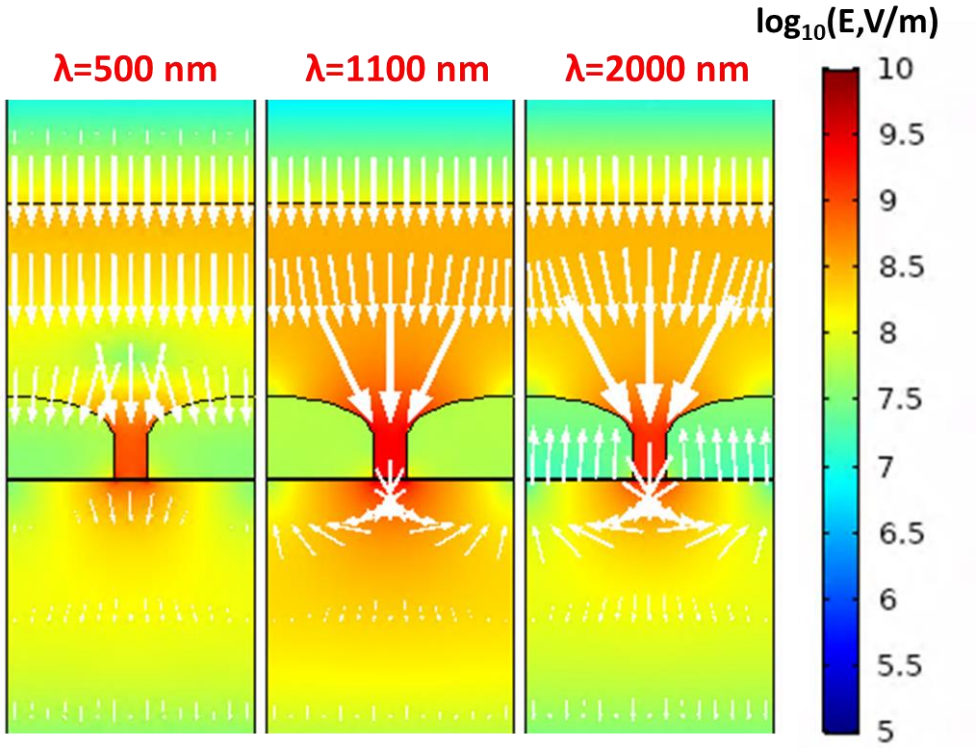

Figure S5 Calculated optical power flow through the Sn/SLG/100 nm SiO_2/Al/quartz framework at different wavelengths using COMSOL Wave Optics Module. The unit of the electric field is V/m. The white arrows indicate the directions and magnitude of the optical power flux in which the arrow length is logarithmic to power flux density. The underneath Al/quartz layers are not presented.

6. Calculated Transmission Spectrum of Sn Nanostructures on Quartz

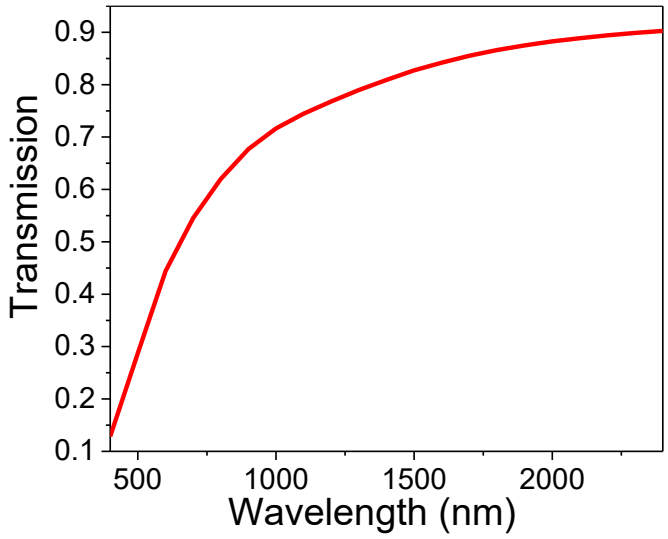

Figure S6 Calculated transmission spectrum of Sn nanostructures on quartz from COMSOL Multiphysics Wave Optics Module using experimentally measured Sn nanostructure geometry. The Sn nanostructures have the same morphological parameters as those deposited on the top of SLG/100 nm SiO_2/Al/quartz.

7. Current-Voltage (I-V) Measurement in Dark Room

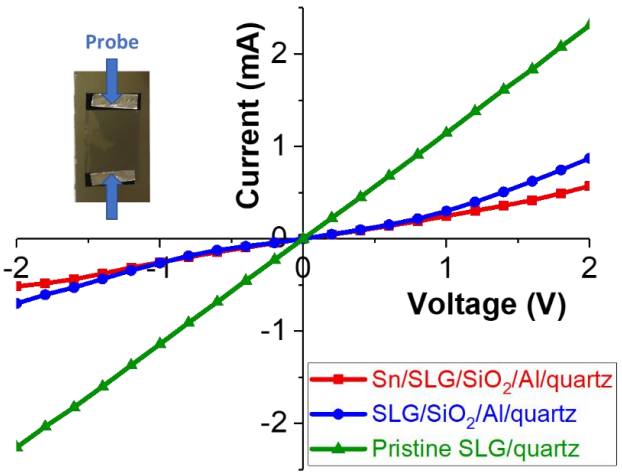

Figure S7 Current-Voltage (I-V) measurement results of pristine SLG/quartz (green line), SLG/SiO_2/Al/quartz structure (blue line), and Sn/SLG/SiO_2/Al/quartz Optical SAC cavity framework (red line) samples under dark environment. The I-V curves of SLG/SiO_2/Al/quartz and Sn/SLG/SiO_2/Al/quartz are not completely linear, possibly due to a small Schottky contact barrier with more intrinsic SLG layers on these samples, as indicated by the Raman analysis in **Figure 3**. The inset shows a photo of the prototype photo-conductor device for demonstration of concept.

8. Optical Absorption of the Sn/SLG/150 nm SiO_2/Al Optical SAC Framework

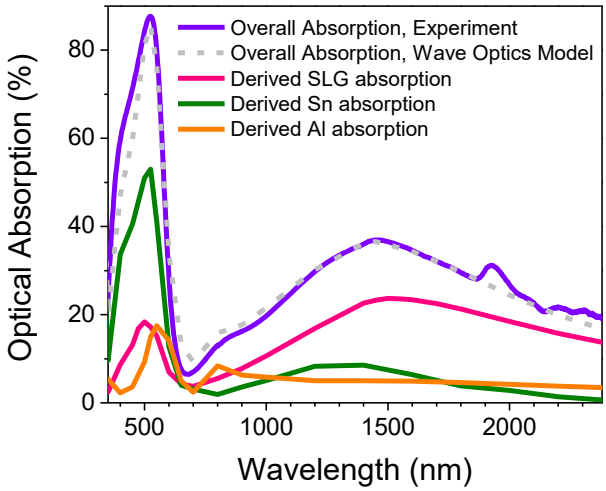

Figure S8 Optical absorption spectra of the Sn/SLG/150 nm SiO_2/Al Optical SAC cavity framework, showing an excellent agreement between the experimentally measured overall absorption spectrum (blue line) and the wave optics modelling (dashed gray line) based on experimentally characterized morphology of the Sn nanostructures and the SiO_2 layer thickness. The detailed breakdown of the optical absorption in SLG (pink line), Sn (green line) and Al (orange line) derived from the wave optics model is also shown in the figure.